

Redshift uncertainties and baryonic acoustic oscillations

Jonás Chaves-Montero, Raúl E. Angulo, & Carlos Hernández-Monteagudo

Centro de Estudios de Física del Cosmos de Aragón, Plaza San Juan 1, Planta-3, 44001, Teruel, Spain.

1 November 2016

ABSTRACT

In the upcoming era of high-precision galaxy surveys, it becomes necessary to understand the impact of uncertain redshift estimators on cosmological observables. In this paper we present a detailed exploration of the galaxy clustering and baryonic acoustic oscillation (BAO) signal under the presence of redshift errors. We provide analytic expressions for how the monopole and the quadrupole of the redshift-space power spectrum (together with their covariances) are affected. Additionally, we discuss the modifications in the shape, signal to noise, and cosmological constraining power of the BAO signature. We show how and why the BAO contrast is *enhanced* with small redshift uncertainties, and explore in detail how the cosmological information is modulated by the interplay of redshift-space distortions, redshift errors, and the number density of the sample. We validate our results by comparing them with measurements from a ensemble of N -body simulations with $8100h^{-3}\text{Gpc}^3$ aggregated volume. Finally, we build a theoretically-motivated template to extract the BAO scale in an unbiased manner relative to the case with no error, and present a quick method to forecast the expected accuracy based on the properties of a given galaxy sample. Our findings suggest that future photometric galaxy surveys offer a huge potential despite the redshift uncertainties intrinsic to their design, and we expect our work to facilitate their complete and optimal exploitation.

Key words: large-scale structure of the Universe

1 INTRODUCTION

A new generation of wide-field cosmological galaxy surveys will soon map the spatial distribution of hundreds of millions of galaxies over a wide range of redshifts. With these, it will be possible to measure the expansion history and structure growth in the Universe with exquisite precision. These measurements can then be used to put strong constraints on the contributors to the total energy density of the Universe, the law of gravity on large scales, and perhaps will offer hints to explain the accelerated expansion of the Universe (see Weinberg et al. 2013, for a review).

Some of these future galaxy surveys will employ high-resolution spectrographs, which will deliver precise estimates for the redshift of galaxies (e.g. DESI, WEAVE, 4MOST). Other surveys, instead, will rely on either low-resolution spectrographs, linear variable filters, or a system of narrow-band filters (e.g. J-PAS, PAU, EUCLID, SphereX). The advantage of the later is that they allow faster mapping speeds and/or that they avoid any target pre-selection. However, this approach adds non-negligible uncertainties in the measured redshifts.

In configuration space, adding uncertainties to the redshift of the galaxies can be regarded as a smoothing operation on the galaxy field along the line-of-sight. Conversely, in Fourier space, they can be regarded as a reduction in the amplitude of line-of-sight modes. Therefore, there is an effective

loss of cosmological information for a survey with a finite number of mass tracers.

The impact of redshift uncertainties on the galaxy clustering and on the baryonic acoustic oscillations (BAO) has been explored by several authors (Seo & Eisenstein 2003; Glazebrook & Blake 2005; Blake & Bridle 2005; Dolney et al. 2006; Seo & Eisenstein 2007; Cai et al. 2009; Benítez et al. 2009; Sereno et al. 2015). These authors showed that an increment in redshift errors leads to a dilution in the BAO signal on small scales due to a decrement in the clustering signal relative to the discreteness (a.k.a shot) noise. Nevertheless, they showed that the BAO scale can still be measured, although with less precision. For instance, as shown by Cai et al. (2009), the uncertainty on the measured acoustic scale doubles for a redshift error of $\sigma_z/(1+z) \sim 0.3\%$. This has motivated surveys such as J-PAS, which aims at delivering a sub-percent redshift accuracy employing a set of 56 contiguous 150\AA -wide filters.

It is clear the cosmological potential of future photometric galaxy surveys despite of the redshift errors and of the strong requirement in terms of photometric calibration and control of systematics. However, the observed clustering of galaxies will be sensitive on how the noise properties of the redshift estimator couple to the intrinsic anisotropic galaxy clustering. Hence, a detailed modelling is necessary to guarantee robust cosmological inferences and an accurate extraction of the information encoded in the BAO signal.

In this paper we develop a complete framework for the exploitation of the BAO signal under the presence of redshift errors. First we provide analytic expressions for how the monopole and the quadrupole of the redshift-space power spectrum (together with their covariances) are affected. Our model is able to capture, within few percent and for all wavelengths explored, these quantities as measured in cosmological N -body simulations.

Then, we explore in detail the signal-to-noise ratio of the BAO wiggles and its cosmological constraining power. We show how and why the BAO contrast is enhanced with small redshift uncertainties, and explore in detail how the cosmological information is modulated by the interplay of redshift-space distortions, redshift errors, and the number density of the sample.

We employ our findings to develop a procedure that can be applied to simulated and/or observed data to extract the BAO scale in an unbiased manner. We present our results for a wide range of galaxy number densities, typical redshift errors, and error distributions. We provide a simple fitting function that captures our numerical results accurately.

Our paper is organized as follows. In §2 we describe the set of cosmological simulations that we use, the way that we compute clustering statistics from these simulations, and how we introduce redshift uncertainties. In §3 we derive analytical expressions for the impact of redshift errors on the shape and variance of the monopole and quadrupole of the power spectrum. Then, in §4, we model how redshift errors alter the BAO feature and the information that they encode. In §5 we build an unbiased model for the BAO wiggles in the power spectrum monopole and apply it to simulated samples with different redshift errors, large-scale biases, probability density functions, and number densities. We conclude and summarize our most important results in §6.

2 NUMERICAL METHODS

2.1 Numerical Simulations

The first N -body calculation employed in this work is the Millennium XXL (hereafter MXXL). The MXXL simulation followed 6720^3 particles of mass $m_p = 8.456 \times 10^9 M_\odot$ inside a cubical region of $L = 3 h^{-1} \text{Gpc}$ on a side. The gravitational forces were computed with a lean version of the **Gadget** code (Springel et al. 2005), and the softening length was set to $10 h^{-1} \text{kpc}$. The cosmological parameters adopted are identical to those of the Millennium Simulation (Springel 2005). Explicitly: $\Omega_m = 0.25$, $\Omega_\Lambda = 0.75$, $\Omega_b = 0.045$, $n_s = 1$, $H_0 = 73 \text{ km s}^{-1} \text{Mpc}^{-1}$, and $\sigma_8 = 0.9$. We refer the reader to Angulo et al. (2012) for more details. Throughout our paper we will employ a catalogue of stellar-mass selected galaxies with a space density of $\bar{n} = 10^{-2} h^3 \text{Mpc}^{-3}$ at $z = 1$, as predicted by a semi-analytic model for galaxy formation carried out on top of the MXXL merger trees (Angulo et al. 2014).

We complement the MXXL results with a suite of 300 simulations with the same volume and cosmological parameters but lower mass resolution. This suite has an aggregated volume of $8100 h^{-3} \text{Gpc}^3$, which is sufficiently large for statistical studies of the BAO signal. For computational efficiency, we carried out these simulations using the Comoving Lagrangian Acceleration (COLA) method (Tassev et al. 2013). The COLA method is able to predict accurately the evolution of the matter density field on intermediate and large

scales at a fraction of the computational cost of a full N -body simulation (Howlett et al. 2015; Koda et al. 2015).

Each COLA simulation evolved 1024^3 particles, each one of mass $1.7 \times 10^{12} h^{-1} M_\odot$, from $z = 9$ down to $z = 1$ using 10 timesteps. The Gaussian initial conditions were created using 2nd order Lagrangian Perturbation theory, and gravitational forces were computed using a Particle-Mesh algorithm with a Fourier grid of 1024^3 mesh points. Each simulation took 3 CPU hours to complete.

Together, the MXXL and the COLA suite will allow us to investigate the impact of redshift uncertainties on the shape of the power spectrum, its variance, and the information content of the BAO scale. Unless otherwise stated, we will explore the $z = 1$ outputs of our calculation, which is motivated by the target redshift range of future wide-field surveys.

2.2 Power spectrum & covariance measurements

Throughout this paper we consider the power spectrum, $P(\mathbf{k})$, defined by:

$$\langle \delta(\mathbf{k})\delta(\mathbf{k}') \rangle = (2\pi)^3 \delta_D(\mathbf{k} + \mathbf{k}') P(\mathbf{k}), \quad (1)$$

where $\langle \rangle$ indicates an ensemble average, $\delta_D()$ is the Dirac delta function, and $\delta(\mathbf{k})$ is the Fourier transform of the density contrast field, $\delta(\mathbf{x})$. Operationally, we compute the power spectrum by Fast Fourier Transforming the distribution of objects in our simulations mapped onto a grid of 1024^3 cells using the cloud-in-cell scheme. We then estimate the anisotropic power spectrum as

$$\tilde{P}(k, \mu) = \frac{1}{N_k} \sum_{\mathbf{k}_i} |\delta(\mathbf{k}_i)|^2, \quad (2)$$

where $k \equiv |\mathbf{k}|$ is the modulus of the \mathbf{k} wave-vector and $\mu = \hat{\mathbf{k}} \cdot \hat{\mathbf{z}}$. The above sum runs over the N_k wave-vectors \mathbf{k}_i that lie within of a set of (k, μ) bins, which we define as equally spaced in $\Delta k = 0.002 h \text{Mpc}^{-1}$ and $\Delta \mu = 0.01$. The respective multipoles thus become

$$P_\ell(k) = \frac{2\ell + 1}{2} \int_{-1}^1 d\mu \tilde{P}(k, \mu) \mathcal{P}_\ell(\mu), \quad (3)$$

where \mathcal{P}_ℓ is the Legendre polynomial of order ℓ . We perform the above integral using the trapezoid rule. Additionally, for the monopole, $\ell = 0$, we apply a first order correction to reduce the contribution of shot noise $P_0(k) \rightarrow P_0(k) - \bar{n}^{-1}$, where \bar{n} is the mean number density of objects considered. Note that such correction assumes that the noise has no frequency dependence and altogether vanishes for the quadrupole, $\ell = 2$, as it does not display an angular dependence.

An ensemble of M power spectrum measurements can be used to compute the corresponding covariance matrix:

$$\mathbf{C}_\ell(k_i, k_j) = \frac{1}{M - 1} \sum_{m=1}^M [P_\ell^m(k_i) - \bar{P}_\ell(k_i)][P_\ell^m(k_j) - \bar{P}_\ell(k_j)], \quad (4)$$

where $P_\ell^m(k_i)$ is the i -th measurement of the power spectrum multipole at the scale k_i , and $\bar{P}_\ell(k_i)$ is the average.

We calculate the precision matrix, \mathbf{C}_ℓ^{-1} , by computing the inverse of $\mathbf{C}_\ell(k_i, k_j)$ using an algorithm based on a LU

factorization. The expected value of \mathbf{C}_ℓ^{-1} when estimated with a finite number of measurement is biased. Following Hartlap et al. (2007), we correct for this as follows:

$$\mathbf{C}_\ell^{-1}(k_i, k_j) \rightarrow \frac{N - N_{\text{bins}} - 2}{N - 1} \mathbf{C}_\ell^{-1}(k_i, k_j), \quad (5)$$

where N_{bins} is the number of k bins. The numerical value of the correction factor for the case of our COLA ensemble ($N = 300$) and the range of k which we use in §5 is 1.496.

2.3 Redshift uncertainties

In our simulations, we model redshift errors and redshift-space distortions in the flat sky approximation, i.e. we perturb the position of objects along the \hat{z} direction, x_z :

$$x_z \rightarrow x_z + (1+z) \frac{v_z}{H(z)} + \delta z \quad (6)$$

where v_z is the physical velocity along the z axis in km s^{-1} , and $H(z)$ the Hubble parameter at redshift z . δz is a random variable whose probability density function (PDF), $\text{Pr}(\delta z)$, is given by the distribution redshift errors.

By default, we will assume that $\text{Pr}(x)$ is a Gaussian distribution with zero mean and standard deviation $\sigma = \sigma_z(1+z)cH^{-1}(z)$, where $\sigma_z(1+z)$ is the typical error in the units of redshift. However, in reality redshift errors may follow non-Gaussian PDFs. For instance, the comparison of photometric and spectroscopic redshifts in the COSMOS survey showed that $\text{Pr}(\delta z)$ is described by a Lorentzian variate (Ilbert et al. 2009). Additionally, $\text{Pr}(\delta z)$ at low redshifts usually shows a tail towards higher redshifts, which is a natural consequence of imposing $z > 0$ in otherwise symmetric PDFs. Therefore, in addition to the Gaussian case, we will consider three families of functional forms for $\text{Pr}(x)$:

- i) Cauchy/Lorentzian: $\text{Pr}(x)dx = \frac{1}{\sigma\pi} \left[1 + \left(\frac{x}{\sigma}\right)^2\right]^{-1} dx$,
- ii) Norm1: $\text{Pr}(x)dx = \frac{1}{2\sigma\Gamma(1+\frac{1}{\beta})} \exp\left(-|x/\sigma|^\beta\right) dx$,
- iii) Norm2: $\text{Pr}(x)dx = \frac{-1}{\kappa x \sqrt{2\pi}} \exp\left[-\frac{1}{2\kappa^2} \log^2\left(-\frac{\kappa x}{\sigma}\right)\right] dx$,

where σ is a parameter that controls the width of the distribution, and Γ is the Gamma function. For the second family of distributions, β controls the excess kurtosis. Distributions with $\beta < 2$ show extended wings like a Lorentzian, whereas with $\beta > 2$ are boxier than a Gaussian. For the third family, κ determines the skewness and the excess kurtosis. Note that we disregard the possibility of interlopers (galaxies systematically assigned to incorrect redshifts due to spectroscopic line misidentification).

3 CLUSTERING WITH REDSHIFT ERRORS

In this section we derive general analytic expressions for the impact of redshift uncertainties on the shape of the monopole and the quadrupole (§3.1) of the power spectrum, and their variances (§3.2). In all cases, we will contrast these predictions with results from numerical simulations.

3.1 The shape of $P_0(k)$ and $P_2(k)$

3.1.1 General expressions

Let us consider a set of galaxies with a real-space density contrast field $\delta_r(\mathbf{k})$ discretely sampling a Gaussian field of covariance $P(\mathbf{k})$ and whose redshifts are measured through a noisy but unbiased estimator. The observed redshifts are thus $z \rightarrow z + \delta z$. Assuming that the PDF of δz , $\text{Pr}(\delta z)$, is identical for every galaxy, we can write the redshift-space overdensity field within the Gaussian dispersion model (Kaiser 1987):

$$\delta_z(k, \mu) = \delta_r(k) \mathcal{F}(k, \mu), \quad (7)$$

$$\mathcal{F}(k, \mu) \equiv (1 + \beta\mu^2) e^{-0.5(\mu k \sigma_v)^2} F(\mu k), \quad (8)$$

where $\beta \equiv b^{-1} d \log D(a) / d \log a$, b is the large-scale bias of the sample, $D(a)$ is the linear growth factor, $a = 1/(1+z)$ is the cosmological scale factor, σ_v is a velocity dispersion induced by non-linear dynamics, $F(\mu k)$ is the Fourier transform of the $\text{Pr}(\delta z)$, and $\mu = \hat{\mathbf{k}} \cdot \hat{\mathbf{z}}$ is the director cosine along the z -axis. Hereafter, for brevity we will not write explicitly the dependence of \mathcal{F} on μ and k .

The relation between P_0^r and P_0 (the monopoles in real and in redshift space, respectively) is:

$$P_0(k) = P_0^r(k) \langle \mathcal{F}^2 \rangle_{\mathbf{k}}, \quad (9)$$

$$\langle \mathcal{F}^2 \rangle_{\mathbf{k}} = \frac{1}{2} \int_{-1}^1 d\mu \mathcal{F}^2. \quad (10)$$

here, and in the remainder of this paper, $\langle \dots \rangle_{\mathbf{k}}$ brackets will denote angular averages (i.e. averages over μ).

Similarly, we can write the quadrupole in redshift space, P_2 , in terms of the monopole in real space:

$$P_2(k) = P_0^r(k) \frac{5}{2} (3 \langle \mu^2 \mathcal{F}^2 \rangle_{\mathbf{k}} - \langle \mathcal{F}^2 \rangle_{\mathbf{k}}). \quad (11)$$

It is straightforward to see how redshift errors create an anisotropic clustering, $P_2 \neq 0$, even if the underlying galaxy field is isotropic. In the general case, redshift errors will couple with the intrinsic redshift-space anisotropies of the galaxy field.

3.1.2 The Gaussian case

In the case of a Gaussian $\text{Pr}(\delta z)$, $F(k\mu) = \exp\{-0.5(\mu k \sigma)^2\}$, with $\sigma = \sigma_z(1+z)cH^{-1}(z)$, there are analytic expressions for $\langle \mathcal{F}^2 \rangle_{\mathbf{k}}$ and $\langle \mu^2 \mathcal{F}^2 \rangle_{\mathbf{k}}$:

$$\begin{aligned} \langle \mathcal{F}^2 \rangle &= \frac{\sqrt{\pi}}{2} \frac{\text{Erf}(x)}{x} \left(1 + \frac{\beta}{x^2} + \frac{3\beta^2}{4x^4}\right) \\ &\quad - \frac{\beta e^{-x^2}}{x^2} \left(1 + \frac{3\beta}{4x^2} \mathcal{H}_1(x)\right), \end{aligned} \quad (12)$$

$$\begin{aligned} \langle \mu^2 \mathcal{F}^2 \rangle &= \frac{\sqrt{\pi}}{4} \frac{\text{Erf}(x)}{x^3} \left(1 + \frac{3\beta}{x^2} + \frac{15\beta^2}{4x^4}\right) \\ &\quad - \frac{\exp(-x^2)}{2x^2} \left(1 + \frac{3\beta}{x^2} \mathcal{H}_1(x) + \frac{15\beta^2}{4x^4} \mathcal{H}_2(x)\right) \end{aligned} \quad (13)$$

where $\mathcal{H}_n(x) = \sum_{i=0}^n \frac{2^i}{(2i+1)!!} x^{2i}$, $!!$ denotes the double factorial, $x = k \sigma_{\text{eff}}$, and $\sigma_{\text{eff}} = \sqrt{\sigma_z^2 + \sigma_v^2}(1+z)cH^{-1}(z)$. To obtain

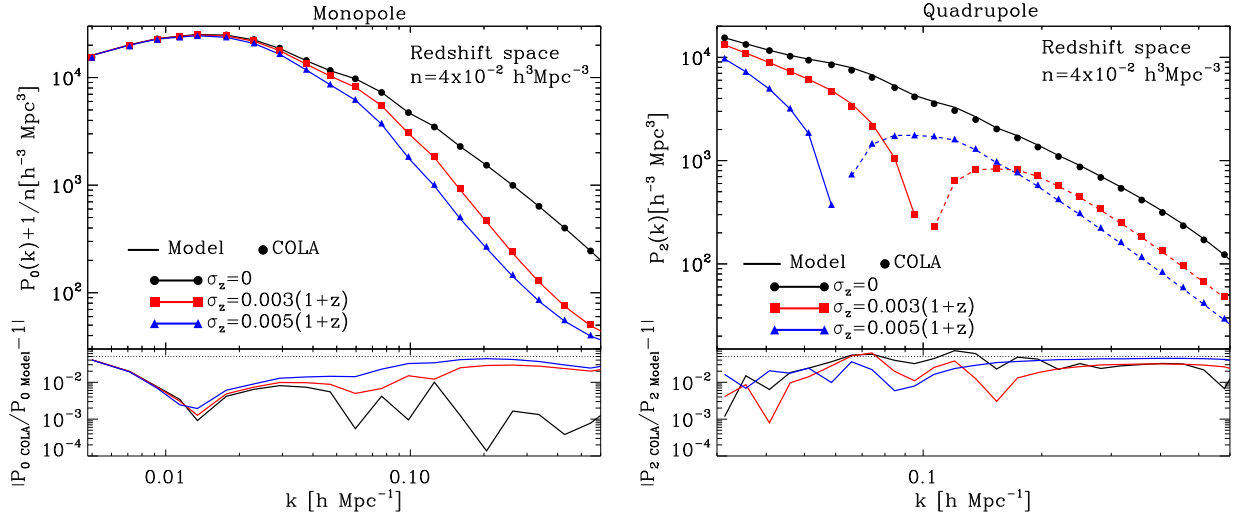


Figure 1. Impact of redshift errors on the monopole (left panel) and quadrupole (right panel) of the power spectrum. Symbols show the average measurement in an ensemble of 300 N -body simulations, whereas solid lines show our analytic prediction for the effect of redshift errors (Eqs. 9–12 for the monopole and Eqs. 11–13 for the quadrupole), which employs as an input the measured real-space clustering and $\sigma_v = 3 \times 10^{-4}$. Different colours show the results for three Gaussian redshift errors of different width, as indicated by the legend. The dashed lines of the right panel denote when the quadrupole is negative. The relative difference between the simulated data and the analytical model is shown in the bottom panels, where the horizontal dotted line indicates a 5% discrepancy level.

these expressions we have assumed that $x > 0$ ¹. The equivalent expressions in real space can be trivially obtained by setting $\beta = 0$. In that case we recover the expression provided in Cai et al. (2009) for the monopole.

It is straightforward to see that redshift errors suppress P_0 and P_2 on all scales, with a stronger suppression for larger wavelengths. In real space, P_0 is suppressed by 1.08 at $k\sigma_{\text{eff}} = 0.5$, whereas redshift errors induce a negative P_2 which is 6.67 times P_0^* on the same scale. In redshift space, redshift errors couple with RSD, thus their net impact depends on β . In general, RSD increase the clustering along the line-of-sight for $k\sigma_{\text{eff}} < 1$ and suppress the clustering on smaller scales. The suppression due to redshift errors is smaller than in real space for scales where $k\sigma_{\text{eff}} > 1$. For instance, considering a sample with $\beta = 1$, the suppression of the power spectrum is 1.77 at $k\sigma_{\text{eff}} = 2$, whereas in real space is 2.27 at $k\sigma = 2$. However, on large scales the net effect of RSD and redshift errors is an increment in the amplitude of the monopole, e.g. it is increased by 1.66 at $k\sigma_{\text{eff}} = 0.5$. Additionally, the small-scale clustering suppression due to redshift errors inverts the sign of the quadrupole on scales $k\sigma_{\text{eff}} > 1$.

3.1.3 Comparison with numerical simulations

In the left panel of Fig. 1 we display the average redshift-space monopole of the DM particles in our COLA ensemble at $z = 1$. We have perturbed those particles following the procedure described in §2.3 to mimic the impact of Gaussian redshift errors. Symbols display three cases with different typical redshift uncertainties, as indicated by the figure. As expected, redshift errors suppress the clustering on small scales, while leaving large scales unaffected. Additionally, the suppression implies

that the larger the redshift error, the larger the scale where the contribution of shot noise becomes important. The predictions of Eq. 12, shown by solid lines, quantitatively capture the relevant effects. The accuracy of the model, quantified in the bottom panel, is within 5% on all scales shown. Note that we employ the measured real-space power spectrum to build this model and we use $\sigma_v = 3 \times 10^{-4}$, which is obtained by finding the value that fits the best the redshift-space monopole power spectrum without redshift errors.

In the right panel of Fig. 1 we show the redshift-space quadrupole power spectrum. Symbols display three cases with different redshift uncertainties, as indicated by the legend. The predictions of Eqs. 11 and 13, shown by solid lines when the quadrupole is positive and by dashed lines when is negative, capture the relevant effects. The accuracy of the model, quantified in the bottom panel, is the same as for the monopole.

3.2 The variance of $P_0(k)$ and $P_2(k)$

3.2.1 General expressions

Redshift errors modify the shape of the power spectrum as well as its variance. The variance of the power spectrum is defined as the diagonal elements of the power spectrum covariance matrix, i.e:

$$\sigma^2[P] = \frac{2}{N_k} \sum_{\mathbf{k}_i} \langle |\delta(\mathbf{k}_i)|^4 \rangle - \langle \tilde{P}(\mathbf{k}_i) \rangle^2, \quad (14)$$

where $\langle \dots \rangle$ denote ensemble averages over multiple realizations/universes. Note the factor of two appears because only half of the modes are independent owing to the reality of $\delta(\mathbf{x})$. The above expression reduces to:

$$\sigma^2[P] = \frac{2}{N_k} \langle P(k) \rangle^2 \quad (15)$$

in the Gaussian limit (i.e. assuming that $\delta_R(\mathbf{k})$ and $\delta_I(\mathbf{k})$ –

¹ Note, however, that Eqs. 12 and 13 diverges as $x \rightarrow 0$. This can be avoided by expanding $F(k\mu)$ into a power series, which yields to alternative expressions valid when $x < 1$, which we provide in Appendix A.

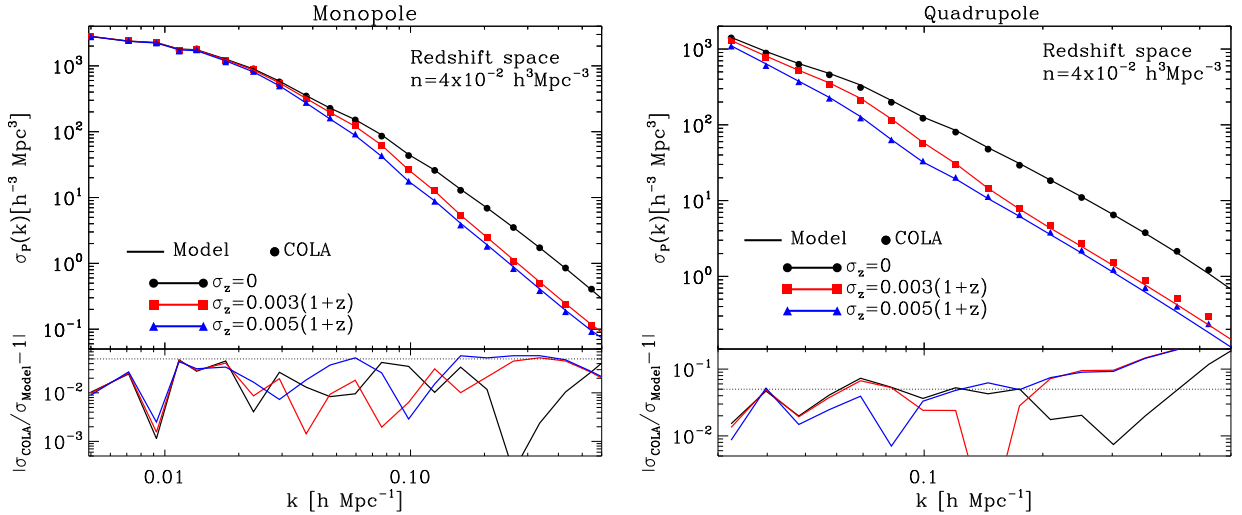


Figure 2. Same as Fig. 1 but for the standard variation of the monopole (left panel) and quadrupole (right panel) of the power spectrum. In this case the numerical data is confronted with the expressions provided by Eqs. 16 and 17 respectively.

the real and imaginary parts of $\delta(\mathbf{k})$, respectively – are Gaussian random variables with zero mean and standard deviation $P(\mathbf{k})/2$.

Combining Eqs. 9 and 14 we obtain an expression for the variance of P_0 under the presence of shot noise and redshift errors:

$$\sigma^2[P_0] = \frac{(P_0^r)^2}{N_k} \left[3\langle \mathcal{F}^4 \rangle_{\mathbf{k}} - \langle \mathcal{F}^2 \rangle_{\mathbf{k}}^2 + \frac{4\langle \mathcal{F}^2 \rangle_{\mathbf{k}}}{\bar{n}P_0^r} + \frac{2}{(\bar{n}P_0^r)^2} \right], \quad (16)$$

We note that in real space and without redshift errors, $\langle \mathcal{F}^2 \rangle_{\mathbf{k}} = \langle \mathcal{F}^4 \rangle_{\mathbf{k}} = 1$, and our expression for the variance reduces to that provided by Colombi et al. (2009).

Similarly, we can compute the variance of P_2 :

$$\sigma^2[P_2] = \frac{25(P_0^r)^2}{4N_k} \left[3\langle (3\mu^2 - 1)^2 \mathcal{F}^4 \rangle_{\mathbf{k}} - \langle (3\mu^2 - 1) \mathcal{F}^2 \rangle_{\mathbf{k}}^2 \right]. \quad (17)$$

The variance of P_2 differs to the variance of P_0 because the terms associated to the shot noise are zero, as we stated in §2.2. Note that P_2 and $\sigma[P_2]$ are both zero in real space without redshift errors [$\langle (3\mu^2 - 1) \mathcal{F}^2 \rangle_{\mathbf{k}} = \langle (3\mu^2 - 1)^2 \mathcal{F}^4 \rangle_{\mathbf{k}} = 0$].

Redshift errors do not modify the covariance structure of the measured density contrast, so in particular if the real-space correlation matrix is diagonal, then so it is in redshift space with or without redshift errors. Hence, there is no extra coupling in Fourier space induced by redshift errors (or linear RSD).

3.2.2 The Gaussian case

For a Gaussian $\text{Pr}(\delta z)$, $\langle \mathcal{F}^4 \rangle_{\mathbf{k}}$, $\langle \mu^2 \mathcal{F}^4 \rangle_{\mathbf{k}}$, and $\langle \mu^4 \mathcal{F}^4 \rangle_{\mathbf{k}}$ have analytic expressions:

$$\begin{aligned} \langle \mathcal{F}^4 \rangle &= \frac{\sqrt{\pi}}{2} \frac{\text{Erf}(x)}{x} \left(1 + \frac{2\beta}{x^2} + \frac{9\beta^2}{2x^4} + \frac{15\beta^3}{2x^6} + \frac{105\beta^4}{16x^8} \right) \\ &\quad - \frac{2\beta \exp(-x^2)}{x^2} \left(1 + \frac{9\beta}{4x^2} \mathcal{H}_1(x) + \frac{15\beta^2}{4x^4} \mathcal{H}_2(x) \right. \\ &\quad \left. + \frac{105\beta^3}{32x^6} \mathcal{H}_3(x) \right), \end{aligned} \quad (18)$$

$$\begin{aligned} \langle \mu^2 \mathcal{F}^4 \rangle &= \frac{\sqrt{\pi}}{4} \frac{\text{Erf}(x)}{x^3} \left(1 + \frac{6\beta}{x^2} + \frac{45\beta^2}{2x^4} + \frac{105\beta^3}{2x^6} + \frac{1890\beta^4}{x^8} \right) \\ &\quad - \frac{\exp(-x^2)}{2x^2} \left(1 + \frac{6\beta}{x^2} \mathcal{H}_1(x) + \frac{45\beta^2}{2x^4} \mathcal{H}_2(x) \right. \\ &\quad \left. + \frac{105\beta^3}{2x^6} \mathcal{H}_3(x) + \frac{1890\beta^4}{x^8} \mathcal{H}_4(x) \right), \end{aligned} \quad (19)$$

$$\begin{aligned} \langle \mu^4 \mathcal{F}^4 \rangle &= \frac{3\sqrt{\pi}}{8} \frac{\text{Erf}(x)}{x^5} \left(1 + \frac{10\beta}{x^2} + \frac{105\beta^2}{2x^4} + \frac{315\beta^3}{2x^6} \right. \\ &\quad \left. + \frac{3465\beta^4}{16x^8} \right) - \frac{3 \exp(-x^2)}{4x^4} \left(\mathcal{H}_1(x) + \frac{10\beta}{x^2} \mathcal{H}_2(x) \right. \\ &\quad \left. + \frac{105\beta^2}{2x^4} \mathcal{H}_3(x) + \frac{315\beta^3}{2x^6} \mathcal{H}_4(x) + \frac{3465\beta^4}{16x^8} \mathcal{H}_5(x) \right) \end{aligned} \quad (20)$$

where $x = \sqrt{2} k \sigma_{\text{eff}}$ and we assume that $x > 0$ to derive these expression². Using them, it is straightforward to construct analytically the variance of P_0 and P_2 .

From the above expressions we can see that redshift errors also reduce the variance of the power spectrum: the values of the first three terms in brackets in the RHS of Eq. 16 are always smaller than their $\sigma_{\text{eff}} = 0$ counterparts since $F(\mu k)$ is always less than unity. On the other hand, the last term in brackets remains unchanged, thus, at a fixed scale, the shot noise contribution progressively dominates as redshift errors increase.

² Note that Eqs. 18, 19, and 20 diverge as $x \rightarrow 0$. In Appendix A we provide valid expressions when $x < 1$.

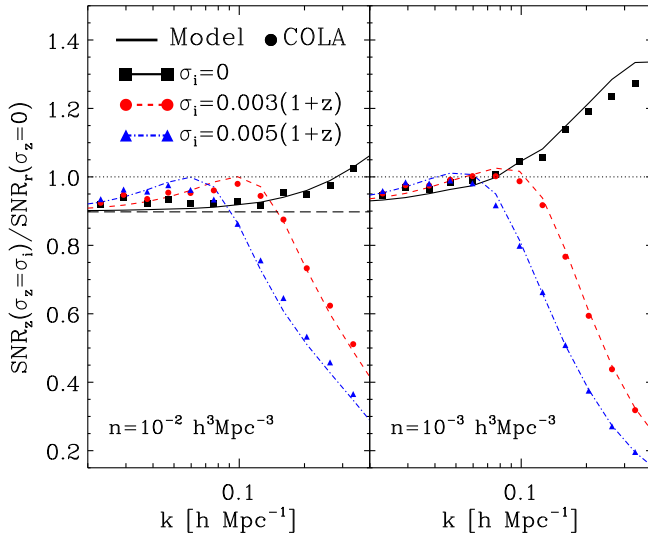


Figure 3. Ratio of the S/N of the redshift-space power spectrum monopole, $P_0/\sigma[P_0]$, to that of a case with no redshift uncertainties in real space, $P_0^r/\sigma[P_0^r]$. Symbols display this quantity computed from our COLA ensemble whereas lines do so for the analytic model of Eqs. 9 and 16. In each panel, black, red, and blue colours represent the cases where $\sigma_z/(1+z) = 0, 0.3\%$, and 0.5% , respectively. For comparison, the horizontal dashed line shows the prediction for the S/N when $\bar{n} \rightarrow \infty$ and $\sigma_v = 0$, i.e. without shot noise and only large-scale RSD.

3.2.3 Comparison with simulations

In the left panel of Fig. 2 we display the variance of P_0 for different redshift uncertainties, as shown by the legend. Symbols indicate measurements from our COLA ensemble for the same samples shown in Fig. 1, whereas solid lines show the prediction of Eq. 16. As for the monopole of the power spectrum, the agreement between our model and the numerical results is remarkable, showing a discrepancy always at or below the 5% level.

In the right panel of Fig. 2 we show the variance of P_2 using the same labelling as the left panel. Symbols show measurements from our COLA ensemble for the same samples shown in Fig. 1, whereas solid lines show the predictions of Eq. 17. In this case, the agreement between our model and the numerical results is within 10% for $k < 0.3 h\text{Mpc}^{-1}$.

3.3 Signal-to-noise ratio for the monopole

Let us now consider the signal-to-noise ratio (S/N) of the redshift-space power spectrum monopole, $P_0/\sigma[P_0]$. The net effect of redshift errors on the S/N is the result of a balance between the suppression induced by redshift errors in the power spectrum monopole and its variance.

3.3.1 Comparison with simulations

We now compare our analytical expressions (i.e. those derived in the previous two subsections) with the results from our ensemble 300 N -body simulations. Specifically, in Fig. 3 we show the S/N relative to that computed in real space without redshift errors. We display results for two number densities and three different redshift uncertainties, as indicated by the

legend. In all cases we can see that our model, indicated by the lines, reproduces fairly well the numerical data, displayed by symbols.

In all three cases and in both the simulated and the analytic results, the S/N converge to the case without redshift errors and non-linear RSD (such case is indicated by the horizontal dashed line) as $k\sigma_{\text{eff}} \rightarrow 0$. Interestingly, this limiting value is $\sim 10\%$ lower than that in real space (indicated by the horizontal dotted line). This implies that, despite the clustering enhancement due to RSD, *the S/N in redshift space is lower than in real space* in the regime where shot noise is subdominant. This is a consequence of the increment in the variance arising from the average of modes with a wider range of amplitudes than in real space.

Additionally, in all cases we appreciate an increase in the S/N relative to the case without redshift errors at a scale of $k\sigma_{\text{eff}} \sim 1$, and a decrease at higher wave-numbers. Interestingly, for $\sigma_z/(1+z) = 0.3\%$, the enhancement occurs at $k \sim 0.15 h\text{Mpc}^{-1}$, the range of scales where BAO are located and thus, it contains relevant cosmological information. As BAO are heavily suppressed by non-linearities and RSD at $k \gtrsim 0.3 h\text{Mpc}^{-1}$, this could imply that stronger cosmological constraints are derived after a smoothing operation. We will return to this in the next section. Overall, these results indicate that, *for scales $k\sigma_{\text{eff}} \sim 1$, the S/N with redshift errors is larger than without errors.*

3.3.2 Toy model

To quantitatively understand the modifications in the S/N of the redshift-space power spectrum monopole due to redshift errors, we build the following toy model:

$$\tilde{P}_0(k) = \frac{1}{2} \tilde{P}_0^r(k) \left(\eta(\mu_1) \exp(-k^2 \sigma^2 \mu_1^2) + \eta(\mu_2) \exp(-k^2 \sigma^2 \mu_2^2) \right). \quad (21)$$

In this expression, the terms in parenthesis provide the contribution of the angular integral at only two μ -values (μ_1, μ_2). The symbol $\tilde{P}_0^r(k)$ denotes the measured power spectrum monopole in real space and $\eta(\mu_{1,2})$ describes the contribution of RSD in the two μ bins. We will assume that $\mu_1 < \mu_2$ and thus $\eta(\mu_1) < \eta(\mu_2)$ since on linear and quasi-linear scales $\eta(\mu)$ should be a monotonically increasing function of μ , and for $\mu = 0$, $\eta(\mu)$ should adopt its real space value, $\eta(\mu = 0) = 1$.

For an ensemble average over a given k bin we have that $\langle \tilde{P}_0(k) \rangle = \frac{P_0^r(k)}{2} [\eta(\mu_1) \exp(-k^2 \sigma^2 \mu_1^2) + \eta(\mu_2) \exp(-k^2 \sigma^2 \mu_2^2)]$, and the S/N per radial k mode reads:

$$\text{S/N} = \frac{1 + \eta_{21} \exp(-k^2 \sigma^2 \Delta \mu^2)}{\sqrt{1 + \eta_{21}^2 \exp(-k^2 \sigma^2 \Delta \mu^2)}}, \quad (22)$$

with $\Delta \mu^2 = \mu_2^2 - \mu_1^2$ and $\eta_{21} = \eta(\mu_2)/\eta(\mu_1)$. From this expression, we shall consider three different cases:

- No redshift errors, $k\sigma = 0$. In this case the S/N is always below $\sqrt{2}$, which is the value corresponding to real space, given by $\eta(\mu) = 1$:

$$\text{S/N} = \frac{1 + \eta_{21}}{\sqrt{1 + \eta_{21}^2}}. \quad (23)$$

- Very large redshift errors, $k\sigma \rightarrow \infty$. Now, the S/N = 1 since all information is lost along the parallel modes.

• Small redshift errors, $k\sigma \rightarrow 0$. In this case we obtain, to first order in $(k\sigma)^2$:

$$S/N = \frac{1 + \eta_{21}}{\sqrt{1 + \eta_{21}^2}} + \frac{\Delta\mu^2 \eta_{21} (\eta_{21} - 1)}{(1 + \eta_{21}^2)^{3/2}} (k\sigma)^2 + \mathcal{O}((k\sigma)^4). \quad (24)$$

That is, in this limit the S/N increases with respect to the case where there are no redshift errors since $\eta_{21} > 1$ in redshift space. This behaviour must thus yield a local maximum in the S/N since for larger $k\sigma$ values we must recover the second case just considered above. This reflects the fact that in this limit the redshift errors affect more the variance than the amplitude of the power spectrum monopole, thus slightly increasing the ratio of these two quantities.

From Eq. 24 above one can also find the value of k corresponding to the local maximum of the S/N, $\partial(S/N)/\partial(k\sigma)^2 = 0$: $(k\sigma)^2 = \log(\eta_{21})/(\Delta\mu^2)$. That is, $(k\sigma)^2 \sim 1$, as shown in Fig. 3.

4 BARYONIC ACOUSTIC OSCILLATIONS WITH REDSHIFT ERRORS

We now investigate the effect of redshift errors on the BAO in Fourier space and the cosmological information they encode.

4.1 The shape of the BAO signal

Let us begin by considering the following quantity:

$$B(k) \equiv \frac{P_0(k)}{P_0^{\text{sm}}(k)} - 1, \quad (25)$$

where P_0^{sm} is a smoothed version of P_0 , i.e. a power spectrum that displays the same broadband shape but no oscillatory features. Therefore, $B(k)$ is insensitive to the overall shape of the observed power spectrum, and isolates the BAO wiggles.

Let us now write a theoretical model for $B(k)$. Motivated by Renormalized Perturbation Theory (Crocce & Scoccimarro 2008)³, the non-linear redshift-space power spectrum can be written as:

$$P(k, \mu) = [P_{0,\text{lin}}(k) G(k, \mu) + P_{\text{mc}}(k)] b^2 \mathcal{F}^2, \quad (26)$$

where b is the large-scale bias, $P_{0,\text{lin}}(k)$ is the linear theory power spectrum monopole in real space, $P_{\text{mc}}(k)$ is the contribution of mode coupling, and $G(k, \mu)$ is a propagator which is well approximated by a 2D exponential function:

$$G(k, \mu) = \exp\left(-\frac{1}{2}[(1 - \mu^2)k^2\sigma_\perp^2 + \mu^2k^2\sigma_\parallel^2]\right), \quad (27)$$

where σ_\parallel and σ_\perp are parameters that control the loss of information due to non-linearities along and perpendicular to the line-of-sight, respectively. Note that $\sigma_\perp < \sigma_\parallel$, i.e. BAO are smeared further along the line-of-sight as a result of non-linear RSD (e.g. Seo & Eisenstein 2007; Sánchez et al. 2008). We then obtain:

³ Note that the smearing of the BAO signal due to non-linearities cannot be captured within the dispersion model, thus we resort to a different modelling than Eq. 9.

$$B(k) = \left(\frac{P_{0,\text{lin}}(k)}{P_{0,\text{lin}}^{\text{sm}}(k)} - 1\right) G_{\text{eff}}(k), \quad (28)$$

$$G_{\text{eff}}(k) = \langle G(k, \mu) \mathcal{F}^2 \rangle_{\mathbf{k}} \langle \mathcal{F}^2 \rangle_{\mathbf{k}}^{-1}, \quad (29)$$

where we have assumed $b^2 \langle \mathcal{F}^2 \rangle_{\mathbf{k}} P_{0,\text{lin}}^{\text{sm}} \approx b^2 \langle \mathcal{F}^2 \rangle_{\mathbf{k}} (P_{0,\text{lin}}^{\text{sm}} G + P_{\text{mc}}^{\text{sm}})$, see Crocce & Scoccimarro (2008).

We recall that brackets denote angular integrals (see §3.1.1). Therefore, BAO are diluted by the weighted average of $G(k, \mu)$ over μ , where the weights are set by the relative suppression of line-of-sight modes caused by redshift errors. We display G_{eff} in the left panel of Fig. 4 for different Gaussian redshift errors assuming $\sigma_\parallel = 10$ Mpc, $\sigma_\perp = 5$ Mpc, $b = 1$, and the value for β expected the cosmology of our N -body simulations. For comparison, we also show $G(k, \mu = 0)$ and $G(k, \mu = 1)$ as dotted and dashed lines, respectively. As we can see, the greater the value of the redshift error, the smaller the contribution of $G(k, \mu \sim 1)$ and $G_{\text{eff}} \rightarrow G(k, \mu \sim 0)$.

This has an interesting consequence. Since $G(k, \mu \sim 1) < G(k, \mu \sim 0)$ owing to non-linear RSD, *redshift errors make BAO appear sharper in the power spectrum monopole*. We explicitly show this in the right panel of Fig. 4, where we display $B(k)$ measured in our COLA ensemble in real and redshift space. In real space, the BAO are the same with and without redshift errors. In redshift space, we find a different behaviour; the BAO wiggles are sharper for the simulated catalogues including redshift errors. Consistently with our previous discussion, we can see that the larger the redshift errors, the sharper the BAO.

4.1.1 The Gaussian case

In the case of Gaussian redshift errors, Eq. 29 has an analytic expression:

$$\langle G(k, \mu) \mathcal{F}^2 \rangle_{\mathbf{k}} = e^{-\frac{1}{2}(k\sigma_\perp)^2} \left[\frac{\sqrt{\pi}}{2} \frac{\text{Erf}(u)}{u} \left(1 + \frac{\beta}{u^2} + \frac{3\beta^2}{4u^4} \right) - \frac{\beta e^{-u^2}}{u^2} \left(1 + \frac{3\beta}{4u} \mathcal{H}_1(u) \right) \right], \quad (30)$$

where $u = k\sqrt{\sigma_{\text{eff}}^2 + \frac{1}{2}(\sigma_\parallel^2 - \sigma_\perp^2)}$ and we assume $u > 0$ ⁴.

It is useful to take the limit of G_{eff} when $\sigma_\parallel \sim \sigma_\perp$ (real space):

$$G_{\text{eff}}(k) \equiv \frac{\langle G(k, \mu) \mathcal{F}^2 \rangle_{\mathbf{k}}}{\langle \mathcal{F}^2 \rangle_{\mathbf{k}}} \sim e^{-\frac{1}{2}(k\sigma_\perp)^2}, \quad (31)$$

where the smoothing of the BAO feature is independent of redshift errors. However, in redshift space $\sigma_\parallel > \sigma_\perp$ and the exponential is weighted by a factor that is greater for larger redshift errors as we can see in the left panel of Fig. 4.

4.2 Cosmological information on the BAO scale

We now explore how the modifications introduced by RSD and redshift errors in the BAO and in P_0 affect the cosmological information encoded in the position of the BAO feature.

Following Ross et al. (2015), let us consider a given

⁴ Note that Eq. 30 diverges as $u \rightarrow 0$. In Appendix A we provide a valid expression when $u < 1$.

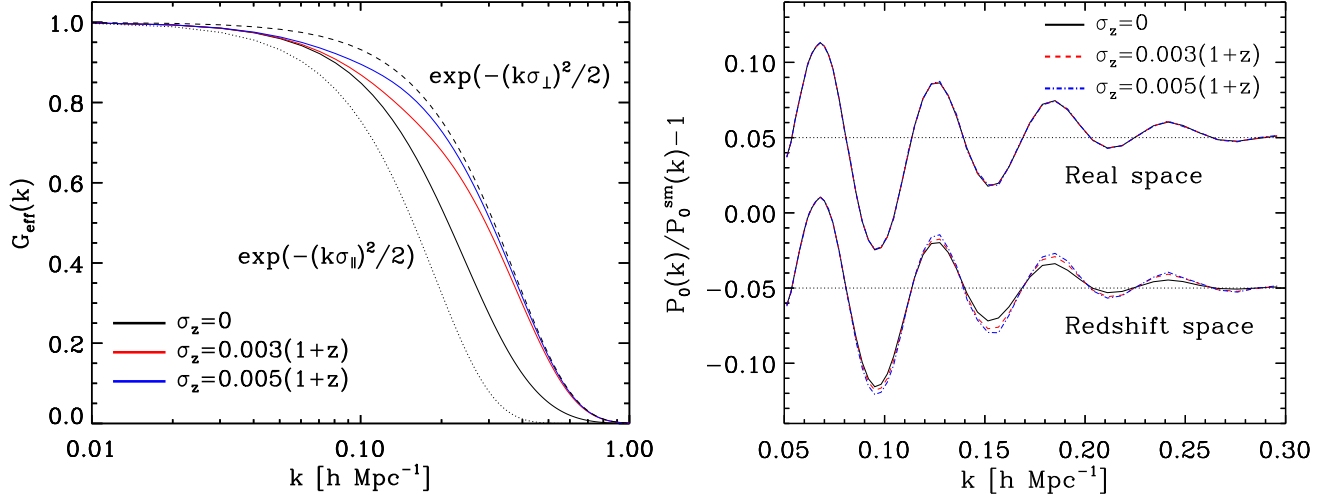


Figure 4. The left panel displays the suppression of the BAO due to non-linearities and RSD, G_{eff} . The colour of the lines indicates G_{eff} for different redshift errors in redshift space, black for $\sigma_z = 0$, red for $\sigma_z/(1+z) = 0.3\%$, and blue for $\sigma_z/(1+z) = 0.5\%$. The dashed line shows the suppression of the BAO for modes perpendicular to the line-of-sight and the dotted line for modes parallel to the line-of-sight. The latter is stronger due to non-linear RSD. Redshift errors increase the weight of modes perpendicular to the line-of-sight, making sharper the BAO scale in redshift space. The right panel shows the average BAO of the COLA ensemble in real and redshift space with different redshift errors. Redshift errors do not modify the BAO wiggles in real-space, whereas they reduce the damping in redshift space, confirming the analytical prediction.

scale in the power spectrum, $k = \sqrt{k_{\parallel}^2 + k_{\perp}^2}$. The observed scale when assuming a fiducial cosmology will be $k' = \sqrt{k_{\parallel}^2 \alpha_{\parallel}^{-2} + k_{\perp}^2 \alpha_{\perp}^{-2}}$, where $\alpha_{\parallel} \equiv H^{\text{fid}}(z)/H(z)$ and $\alpha_{\perp} \equiv D_A(z)/D_A^{\text{fid}}(z)$. In the above expressions, $D_A(z)$ is the angular diameter distance, $H(z)$ is the Hubble parameter, and the fid superscripts denote these quantities computed in the fiducial cosmology.

The observed monopole is thus $P_0(k') = P_0(k/\alpha)$, where

$$\alpha = \left\langle \mathcal{F}^2 \sqrt{\mu^2 \alpha_{\parallel}^2 + (1 - \mu^2) \alpha_{\perp}^2} \right\rangle_{\mathbf{k}}. \quad (32)$$

Expanding the solution to first order, we obtain $\alpha = \alpha_{\parallel}^m \alpha_{\perp}^n$, where m and n are given by:

$$m(k) \equiv \frac{\partial \langle \alpha \rangle}{\partial \alpha_{\parallel}} \bigg|_{\alpha_{\parallel} = \alpha_{\perp} = 1} = \frac{\langle \mu^2 \mathcal{F}^2 \rangle_{\mathbf{k}}}{\langle \mathcal{F}^2 \rangle_{\mathbf{k}}}, \quad (33)$$

$$n(k) \equiv \frac{\partial \langle \alpha \rangle}{\partial \alpha_{\perp}} \bigg|_{\alpha_{\parallel} = \alpha_{\perp} = 1} = \frac{\langle \mathcal{F}^2 \rangle_{\mathbf{k}} - \langle \mu^2 \mathcal{F}^2 \rangle_{\mathbf{k}}}{\langle \mathcal{F}^2 \rangle_{\mathbf{k}}}, \quad (34)$$

where the denominators ensure that $m(k) + n(k) = 1$. Note that the higher the value of m , the more sensitive α is to the Hubble parameter. For the case of Gaussian redshift errors, $m(k)$ and $n(k)$ have analytic expressions given by Eqs. 12-13.

Note the known case $m = 1/3$ and $n = 2/3$ (Eisenstein et al. 2005) is recovered only in real-space (when $\beta = \sigma_v = \sigma = 0$). In redshift space, there is a dependence of m and n on β even if $\sigma = \sigma_v = 0$. In such case, our expressions reduce to the scale-independent formulae presented in Ross et al. (2015). However, as we can see in the general case presented here, non-linear RSD break the scale independence even in the case without redshift errors.

In general, redshift errors and non-linear RSD decrease the sensitivity of the measured P_0 on $H(z)$, whereas large-scale RSD increase its sensitivity as a consequence of the line-of-

Table 1. Degeneracy between the parallel and perpendicular component of α at different scales for samples in redshift space with different b and σ_z . We only include the value of m in the table because $n = 1 - m$.

$k[h \text{ Mpc}^{-1}]$	$\sigma_z/(1+z)[\%]$	$m(b=1.5)$	$m(b=2.5)$
0.1	0 ^a	0.417	0.386
0.2	0 ^a	0.413	0.382
0.1	0.3	0.309	0.283
0.2	0.3	0.125	0.116
0.1	0.5	0.177	0.162
0.2	0.5	0.041	0.040

^a Note that for $\sigma_z = 0$, $\sigma_{\text{eff}} = \sigma_v$ due to RSD. If $\sigma_{\text{eff}} = 0$, we would not find a dependence of m on the scale.

sight clustering enhancement. Therefore, because the relative strength of these effects depends on the scale considered, the magnitude of the redshift error, and the clustering properties of the underlying sample; the exact degeneracy between α_{\parallel} and α_{\perp} (and thus the whole information content of P_0 under redshift errors) will depend on those details.

In Table 1 we provide the value of m at different scales for samples with several combinations of large-scale bias and redshift errors. We see that the lower the large-scale bias of the sample, the stronger the constraints on the line-of-sight component of the BAO and thus, on the Hubble parameter. For samples with redshift errors, we find that on large scales ($k\sigma_{\text{eff}} < 1$) these constraints are similar to those in the absence of errors, however, they are considerably weaker as smaller scales are considered.

Following a similar procedure as the one employed to compute the dependence of α on the perpendicular and radial components, we can compute

$$\langle \alpha^2 \rangle = m(k) \alpha_{\parallel}^2 + n(k) \alpha_{\perp}^2, \quad (35)$$

which can be used to relate the precision in measuring a scale

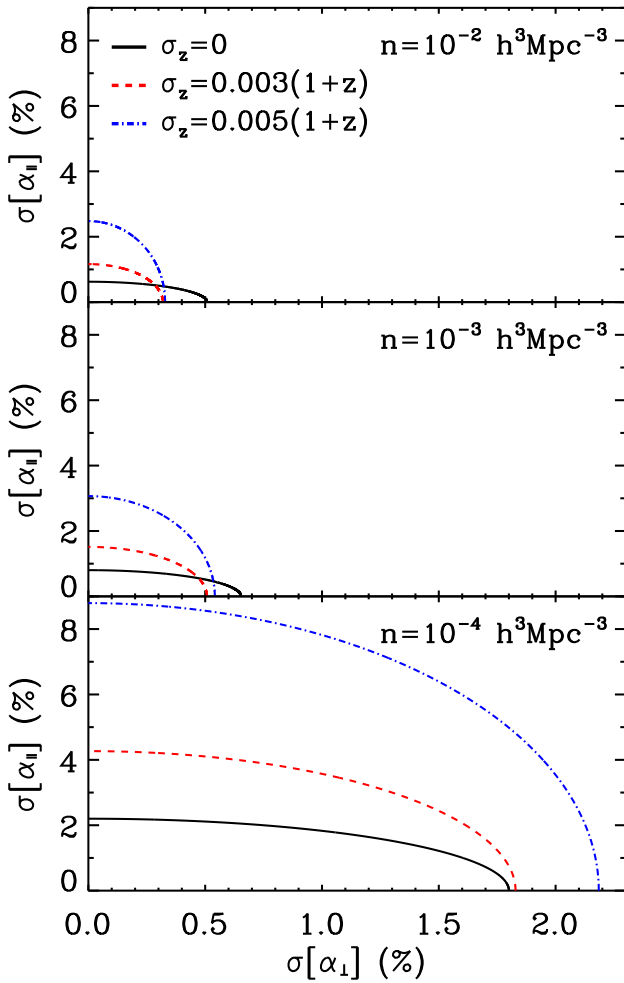


Figure 5. Degeneracy between the standard deviation of α_{\parallel} and α_{\perp} in redshift space for samples with different number densities: $n = 10^{-2} h^3 \text{Mpc}^{-3}$ (top panel), $n = 10^{-3} h^3 \text{Mpc}^{-3}$ (medium panel), and $n = 10^{-4} h^3 \text{Mpc}^{-3}$ (bottom panel). Ellipses enclose the 1σ region and their colour indicates the redshift error, black for $\sigma_z = 0$, red for $\sigma_z/(1+z) = 0.3\%$, and blue for $\sigma_z/(1+z) = 0.5\%$. We draw these ellipses using Eq. 36, compute the values of m_{eff} with and Eq. 37, and use the values of σ_{α} from Table 3.

in the power spectrum to the precision in the radial and perpendicular component $\sigma_{\alpha_{\parallel}}$ and $\sigma_{\alpha_{\perp}}$, respectively:

$$\sigma_{\alpha}^2 = m(k)^2 \sigma_{\alpha_{\parallel}}^2 + n(k)^2 \sigma_{\alpha_{\perp}}^2. \quad (36)$$

4.3 The scale-dependence of cosmological information

The scale dependence of m and n introduces a complication while extracting information from BAO analyses, which combine a relatively wide range of scales (typically from $k \sim 0.01 h\text{Mpc}^{-1}$ to $k \sim 0.3 h\text{Mpc}^{-1}$).

We estimate the effective cosmological dependence as a S/N weighted average of $m(k)$. Explicitly,

$$m_{\text{eff}} = \frac{\int dk m(k) \frac{P_0 G_{\text{eff}}}{\sigma[P_0]}}{\int dk \frac{P_0 G_{\text{eff}}}{\sigma[P_0]}}, \quad (37)$$

where the lower limit of the integrals are set to $0.05 h\text{Mpc}^{-1}$ and the upper limit to $0.3 h\text{Mpc}^{-1}$. Finally, note that the factor G_{eff} captures the suppression in amplitude of the BAO and thus the loss of constraining power of high wavenumbers.

We display in Fig. 5 the degeneracy between $\sigma_{\alpha_{\parallel}}$ and $\sigma_{\alpha_{\perp}}$ in redshift space. From top to bottom, the panels displays results for $\bar{n} = 10^{-2} h^3 \text{Mpc}^{-3}$, $\bar{n} = 10^{-3} h^3 \text{Mpc}^{-3}$, and $\bar{n} = 10^{-4} h^3 \text{Mpc}^{-3}$. Different colours indicate different redshift errors. The area of the ellipses are set by the total error in α in each case.

In the case of no redshift errors, there is almost no scale dependence in m and n ⁵. Thus the ratio of the major and minor semi-axes of the ellipses are identical in all panels. In the case with redshift errors, the shape of the ellipses is modified in a way that also depends on the number density. For a low number densities, there is only cosmological information on large scales, which are also less affected by redshift errors. Hence the shape of the ellipses approach that of the no redshift error case. As we consider larger number densities, smaller scales can be exploited. These scales, in turn, are more affected by redshift errors and thus, there is a loss of information regarding the line-of-sight clustering. Consequently, ellipses become more elongated on the parallel direction.

The above highlights the need for a sophisticated and accurate modelling of the relevant physical and observational effects when interpreting BAO constraints in photometric galaxy surveys.

5 EXTRACTING THE BAO INFORMATION

In the previous section we showed how redshift errors modify the shape of $P_0(k)$, its variance, and the BAO feature. We now employ that information to create a model to extract the BAO scale from observational and/or simulated data, even under the presence of redshift errors. We discuss our model and its motivation in §5.1. We then describe our fitting procedure in §5.2, and in §5.3 we present and discuss the results of applying it to our simulated catalogues.

5.1 Modelling the monopole of the power spectrum

Based in the expressions provided in §3 and §4.1, we can write the following model for the observed power spectrum monopole under the presence of non-linearities, RSD, and redshift uncertainties:

$$P_T(k, \alpha, k_*) = P_{0,\text{obs}}^{\text{sm}}(k) [B_{\text{model}}(k/\alpha, k_*) + 1] \quad (38)$$

where α , which is introduced in §4.2, is equal to unity only if the length scale encoded in $B(k)$ matches that of the fiducial cosmology⁶. In §4 we showed that over the range of scales where we expect most of the BAO signal to reside ($k\sigma_{\text{eff}} < 1$), G_{eff} can be approximated by a Gaussian function with an effective suppression scale (see Eq. 31). Thus we model

$$B_{\text{model}}(k, k_*) = \left[\frac{P_{\text{lin}}(k)}{P_{\text{lin}}^{\text{sm}}(k)} - 1 \right] \exp\left(-\frac{k^2}{2k_*^2}\right), \quad (39)$$

⁵ There no scale dependence in real space. However, in redshift space there is a very small scale dependence due to non-linear RSD.

⁶ This is not strictly correct as the contribution of mode coupling in Eq. 26 introduces a small shift in α (Crocce & Scoccimarro 2008).

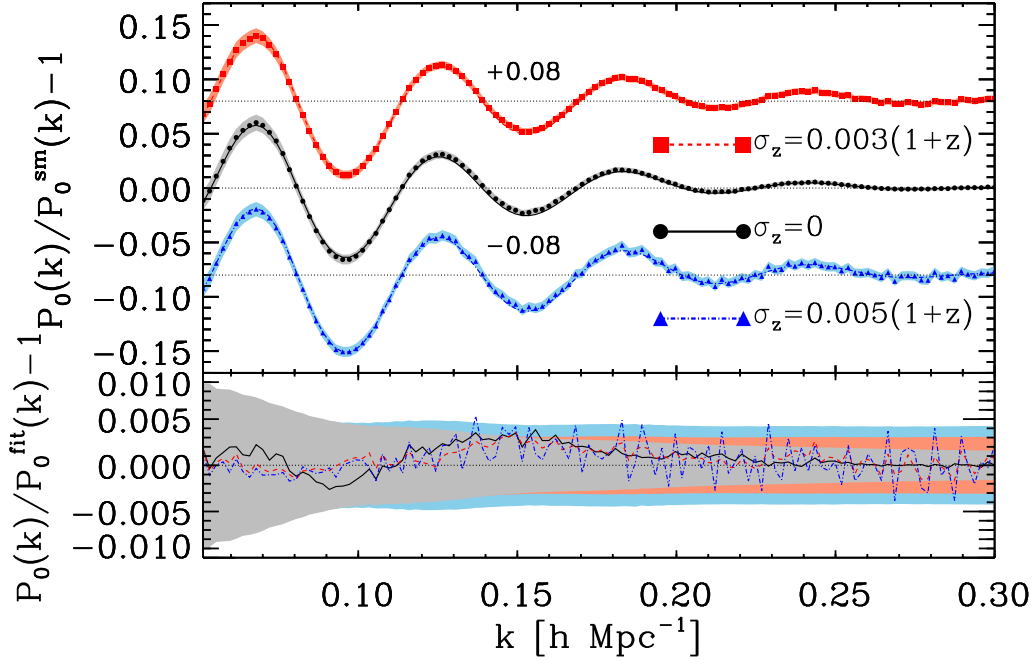


Figure 6. Ratio of P_0 to a smooth version of P_0 without BAO. The data points display the average redshift-space power monopole computed from the ensemble of COLA simulations and the lines indicate the best fit to those points using the model introduced in Eq. 38. The colour indicates the redshift error, black for $\sigma_z = 0$, red for $\sigma_z/(1+z) = 0.3\%$, and blue for $\sigma_z/(1+z) = 0.5\%$. Coloured regions enclose the area between the 84th and 16th percentiles. The bottom panel shows the relative difference of the average monopole from the simulations and the fits.

where k_* is a combination of the BAO dilution factors due to redshift errors, non-linearities, and RSD. Note that this expression is independent of redshift errors (they appear just in k_*) and thus, it is similar to the template employed in the analysis of SDSS data (e.g. Percival et al. 2007, 2010; Anderson et al. 2012). Furthermore, the free parameters of the model only enter in the expression for $B(k)$. Therefore, these parameters are only constrained by BAO information, i.e. the model P_T extracts the BAO scale regardless of the overall power spectrum shape.

5.2 Parameter Likelihood Calculation

We assume that the probability of observing $\mathbf{d} = P_{0,\text{obs}}(k)$ is given by a multivariate Gaussian distribution:

$$\Pr(\mathbf{d}|\pi) \propto \exp \left\{ -\frac{1}{2} [\mathbf{d} - P_T(k, \pi)]^t \mathbf{C}^{-1} [\mathbf{d} - P_T(k, \pi)] \right\}, \quad (40)$$

where $\pi = \{\alpha, k_*\}$ are the parameters of the model P_T given by Eq. 38. The priors on these parameters are assumed to be flat over the range: $\alpha \in [0.93, 1.07]$ and $k_* \in [0.05, 0.8]$. \mathbf{C}^{-1} is the data precision matrix⁷, which we compute from our COLA measurements as described in §2.2. The range of scales considered is $k = (0.05 - 0.30) h \text{ Mpc}^{-1}$. We do not employ smaller scales since BAO wiggles are practically washed out at higher k values due to non-linearities and shot noise.

We sample the posterior probability distribution function of π employing the publicly available code `emcee`

(Foreman-Mackey et al. 2013). This code is an affine invariant MCMC ensemble sampler which has been widely tested and used in multiple scientific studies. We configure the code to analyse the monopole of the power spectrum with a chain of 100 random walkers with 5 000 steps each and a burning phase of 500 steps. We check that this burning phase is sufficient to obtain well-behaved chains.

Additionally, we have checked that the standard deviations of the best fit values from the COLA ensemble are compatible with the uncertainties estimated from the MCMC analysis for each one of our simulated catalogues.

5.3 Extracting the BAO scale from simulated catalogues

In Fig. 6 we show the quality of the best fit model when applied to the COLA ensemble. Symbols show the average measured $B(k)$ in redshift space, whereas lines show the average best fit model. We display three cases for different σ_z values, which have been offset from one to another for clarity. Shaded areas indicate the 1σ region computed from the ensemble of COLA simulations. In all cases, the typical deviations between the data and the best fit model are statistically insignificant. Therefore, the model of Eq. 39 is indeed a very good description of the measured power spectra, as can be best seen in the bottom panel of this figure. We now explore quantitatively the results from the best fit in a wide range of conditions.

5.3.1 The impact of redshift errors

We start by presenting the distribution of best fit values, (α, k_*) , for 300 independent catalogues of dark matter par-

⁷ We show in §B we obtain the same results using analytical precision matrices computed from the inverse of Eq. 16.

Table 2. Result of the MCMC analysis of the ensemble of COLA simulations for $n = 10^{-2} h^3 \text{Mpc}^{-3}$. We show the mean value of α and its error, the average σ_α , and the mean value of k_* and its error.

$\sigma_z/(1+z)(\%)$	$\bar{\alpha} - 1(\%)$	$\bar{\sigma}_\alpha(\%)$	\bar{k}_*
Real space			
0.0	0.19 ± 0.011	0.19	0.1637 ± 0.0003
0.3	0.18 ± 0.013	0.24	0.1658 ± 0.0004
0.5	0.17 ± 0.016	0.30	0.1671 ± 0.0005
Redshift space			
0	0.27 ± 0.016	0.28	0.1248 ± 0.0002
0.3	0.24 ± 0.014	0.25	0.1437 ± 0.0003
0.5	0.18 ± 0.016	0.29	0.1565 ± 0.0004

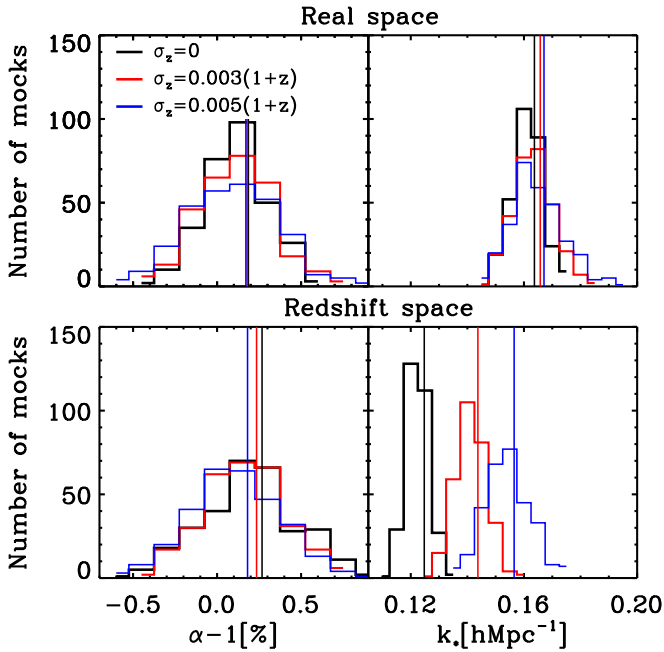


Figure 7. The top panels show the values of α and k_* resulting from the analysis of the ensemble of COLA simulations with $n = 10^{-2} h^3 \text{Mpc}^{-3}$ in real space. The colour of the lines indicates the redshift error, black for $\sigma_z = 0$, red for $\sigma_z/(1+z) = 0.3\%$, and blue for $\sigma_z/(1+z) = 0.5\%$. The bottom panels show the results in redshift space. The value of k_* is compatible for the different redshift errors in real space. However, k_* is greater for larger redshift errors in redshift space, consequence of a weaker suppression of the BAO (see §4).

ticles with $n = 10^{-2} h^3 \text{Mpc}^{-3}$ extracted from our COLA ensemble. We provide these results in Table 2. In Fig. 7 we show histograms of the distribution of best fit values. Top panels show the results in real space whereas bottom panels do so for redshift space. Different colours indicate different redshift errors, as indicated by the legend.

The left panels of Fig. 7 show that the mean of the best fit α values is statistically compatible between the cases with different redshift uncertainties. This implies that *our estimator is unbiased relative to the case without redshift errors*. The mean α value, however, is different than unity by $\sim 0.2\%$. Average values are $\bar{\alpha} \sim 1.0018$ and $\bar{\alpha} \sim 1.0023$ in real and redshift space, respectively. This small shift is caused by mode coupling

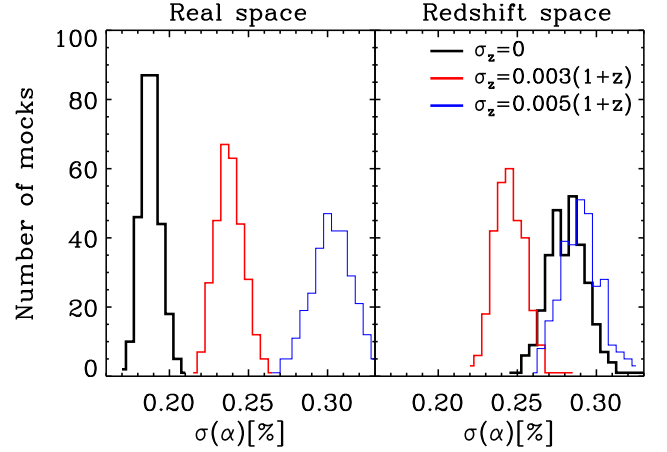


Figure 8. Error in α from the analysis of 300 COLA simulations with $n = 10^{-2} h^3 \text{Mpc}^{-3}$ in real space (left panel) and redshift space (right panel). We use the same colour coding as Fig. 7. In real space, σ_α increases with the redshift error. On the other hand, in redshift space it is smaller for the samples with $\sigma_z/(1+z) = 0.3\%$ than for the samples without redshift errors (see text).

induced by the non-linear gravitational evolution of the mass density field (e.g. Angulo et al. 2008; Crocce & Scoccimarro 2008; Smith et al. 2008; Padmanabhan & White 2009). However, it can in principle be corrected for with reconstruction algorithms (e.g. Eisenstein et al. 2007; Schmittfull et al. 2015) or with a recalibration of the α estimator.

In real space, the distribution of best fit k_* values is compatible across catalogues with different redshift errors. In redshift space, however, k_* depends strongly on redshift errors with larger values for larger redshift errors, i.e. the larger the redshift errors the shaper the BAO wiggles. This can be understood by our analytic discussion presented in §4.1. Redshift errors effectively suppress the contribution of the BAO signal along the line-of-sight. In real space, BAO are isotropic, thus redshift errors do not change the value of k_* , whereas in redshift space, BAO are more diluted along the line-of-sight, thus k_* prefers larger values when redshift errors are added.

We now consider the accuracy in the estimation of α . We display our results in Fig. 8. In real space (left panel), the total error in α increases with increasing redshift error. For $\sigma_z/(1+z) = 0.3\%$, α is estimated with a $\sim 30\%$ less certainty than the $\sigma_z = 0$ case. Since the BAO shape is independent of the redshift errors, the total S/N is reduced by an increase in the noise owing to the shot noise contribution becoming comparatively more important (see §3). In redshift space, the uncertainty in α is a non-monotonic function of the redshift error. For $\sigma_z/(1+z) = 0.3\%$ the error decreases relative to the no redshift error case, whereas for $\sigma_z/(1+z) = 0.5\%$, the error increases. This can be understood as a balance of two effects. The overall S/N increases at scales $k\sigma \sim 1$ and decreases on higher wavenumbers due to the increased shot noise contribution. Therefore, a larger or smaller uncertainty depends on the wavelength where $k\sigma \sim 1$ relative to the BAO scales. For $\sigma_z/(1+z) = 0.3\%$, this occurs at $k \sim 0.2$ – the relevant BAO scales – thus we expect stronger constraints on α . On the other hand, for $\sigma_z/(1+z) = 0.5\%$ this occurs at $k \sim 0.1$, which implies that a considerable fraction of the BAO signal is measured with lower S/N.

In addition to the above effect, in redshift space the BAO

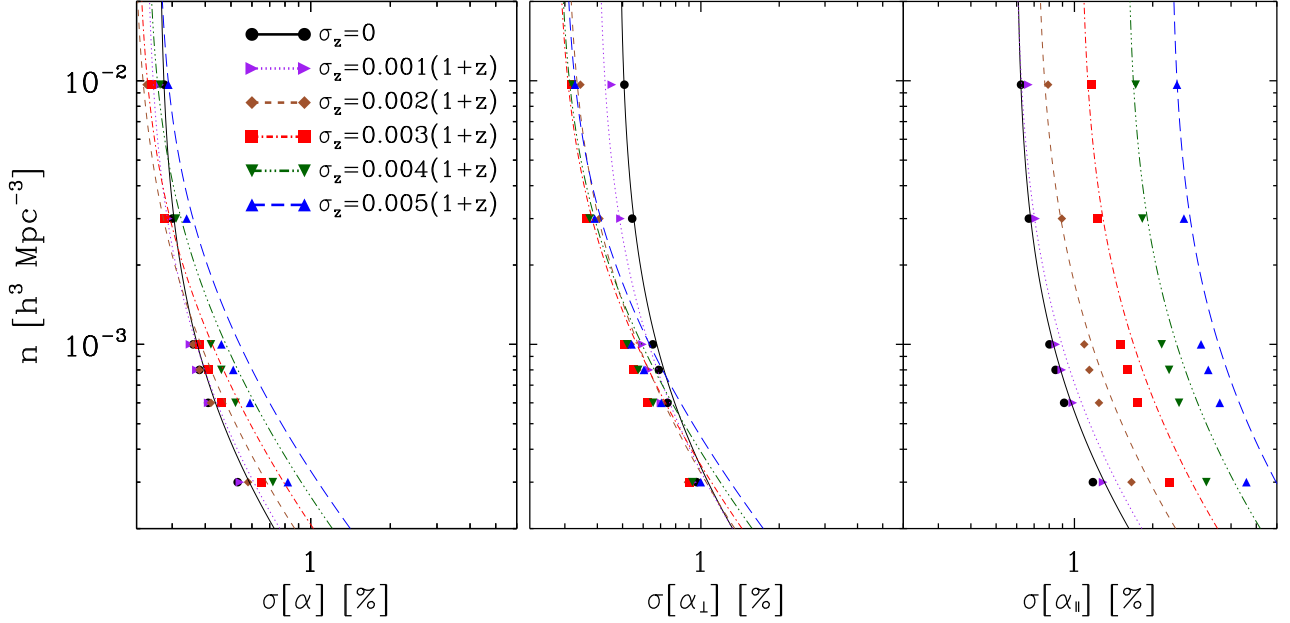


Figure 9. Precision extracting α (left panel), α_{\perp} (middle panel), and α_{\parallel} (right panel) in redshift space from samples with different large-scale bias, number density, and redshift errors. The symbols show the error in the best fit of α computed from the mean of 300 COLA simulations. The colour indicates the redshift error, black for $\sigma_z = 0$, magenta for $\sigma_z/(1+z) = 0.1\%$, brown for $\sigma_z/(1+z) = 0.2\%$, red for $\sigma_z/(1+z) = 0.3\%$, green for $\sigma_z/(1+z) = 0.4\%$, and blue for $\sigma_z/(1+z) = 0.5\%$. The lines show the analytical prediction for the error α using Eq. 41.

signal becomes sharper with redshift errors, increasing the constraining power. However, we have checked that this effect is less important.

5.3.2 The impact of number density

In the previous section we argued how the constraining power of the BAO wiggles is a balance of the redshift errors and the shot noise. Now, we will quantitatively investigate this.

We apply our fitting procedure to seven samples different number densities: $\bar{n} = [10^{-2}, 3 \times 10^{-3}, 10^{-3}, 8 \times 10^{-4}, 6 \times 10^{-4}, 3 \times 10^{-4}, 10^{-4}] \times h^3 \text{Mpc}^{-3}$. Each sample is built by diluting the dark matter particles in our COLA ensemble. Furthermore, we consider redshift uncertainties from $\sigma_z = 0$ to $\sigma_z/(1+z) = 0.5\%$ in steps of $\sigma_z/(1+z) = 0.1\%$ for each case.

We present our results in Table 3. First, we see that the mean value of α is independent on the number density of the sample, which supports the robustness of our analysis procedure. Second, there is a trend with the bias in α being smaller for larger redshift errors. This is likely a consequence of larger redshift errors implying that the constrains on α come from larger, more linear, scales.

The uncertainty in α is shown in the left panel of Fig. 9. For high number densities, the relation between σ_{α} and σ_z is non monotonic as discussed previously. As we consider lower number densities, the uncertainty in α increases for all values of σ_z but it does so more rapidly for larger values of σ_z . At the typical densities of spectroscopic redshift surveys (i.e. SDSS-III/BOSS), $\bar{n} \sim 3 \times 10^{-4} h^3 \text{Mpc}^{-3}$, the error in α increases monotonically with the redshift errors – $\sim 20(45)\%$ larger for $\sigma_z/(1+z) = 0.3(0.5)\%$, respectively. Conversely, to reach the same accuracy on α , the number density should be 50 % larger

for $\sigma_z/(1+z) = 0.3\%$ and 2.5 times larger for $\sigma_z/(1+z) = 0.5\%$.

On the other hand, the uncertainty is different for the angular diameter distance, which depends on the power spectrum modes perpendicular to the line-of-sight, than for the Hubble parameter, which depends on the power spectrum modes parallel to the line-of-sight. We can see this in the right panels of Fig. 9, which show the dependence of the accuracy of the radial and perpendicular components of α on the number density and the redshift errors. Note that for constructing this figure we have employed Eq. 37, where we have adopted the effective values of m and n corresponding to each case.

We can see that a modest increase in the number density already delivers constrains comparable to those of the no redshift error case. At $\bar{n} \sim 3 \times 10^{-4} h^3 \text{Mpc}^{-3}$, the constrains on α_{\perp} for all the cases shown are almost identical. On the other hand, a considerable increase in \bar{n} is necessary to reach comparable constrains on α_{\parallel} ; the number density should be $\sim 3(20)$ times larger for $\sigma_z/(1+z) = 0.2(0.3)\%$.

All the above considerations should be taken into account for the optimal design of a survey or a target sample. For instance, the redshift error of a given galaxy sample might not only depend on the hardware employed, but also on the intrinsic galaxy properties (e.g. brighter objects having more accurate redshift estimates). In such case, the sample that delivers the strongest constrains is not necessarily that with the smallest redshift error.

5.3.3 The impact of biased tracers

The effect of the large-scale bias in real space is straightforward: it increases the amplitude of the power spectrum in all scales, thus reducing the relative contribution of the shot

Table 3. Results of the MCMC analysis of the ensemble of COLA simulations for different number densities and redshift errors. We show the average value of α and σ_α .

\bar{n} [$h^3\text{Mpc}^{-3}$]	$\sigma_z/(1+z)(\%)$					
	0.0	0.1	0.2	0.3	0.4	0.5
1×10^{-2}	0.27 ± 0.28	0.25 ± 0.27	0.25 ± 0.24	0.23 ± 0.25	0.20 ± 0.27	0.18 ± 0.29
3×10^{-3}	0.25 ± 0.30	0.24 ± 0.29	0.23 ± 0.28	0.22 ± 0.28	0.20 ± 0.31	0.18 ± 0.34
1×10^{-3}	0.27 ± 0.36	0.24 ± 0.35	0.23 ± 0.36	0.22 ± 0.38	0.18 ± 0.42	0.17 ± 0.46
8×10^{-4}	0.24 ± 0.38	0.23 ± 0.37	0.21 ± 0.38	0.19 ± 0.41	0.16 ± 0.46	0.15 ± 0.51
6×10^{-4}	0.25 ± 0.41	0.25 ± 0.41	0.23 ± 0.42	0.20 ± 0.46	0.18 ± 0.52	0.15 ± 0.59
3×10^{-4}	0.27 ± 0.53	0.26 ± 0.54	0.23 ± 0.58	0.18 ± 0.65	0.10 ± 0.72	0.04 ± 0.82
1×10^{-4}	0.30 ± 0.99	0.22 ± 1.00	0.22 ± 1.11	0.37 ± 1.28	0.20 ± 1.49	0.21 ± 1.75

Table 4. Results of extracting the BAO information from several samples of the MXXL simulation in redshift space with different number density and large-scale bias.

$\sigma_z/(1+z)(\%)$	$\alpha - 1(\%)$	$\sigma_\alpha(\%)$	k_*	b
$5 \times 10^{-3} h^3\text{Mpc}^{-3}$				
0	0.11	0.26	0.132	1.37
0	0.17	0.26	0.128	1.58
0.3	0.24	0.24	0.157	1.37
0.3	0.29	0.24	0.153	1.58
0.5	0.23	0.29	0.167	1.37
0.5	0.27	0.28	0.167	1.58
$10^{-3} h^3\text{Mpc}^{-3}$				
0	-0.04	0.29	0.134	1.34
0	0.10	0.29	0.125	1.84
0.3	0.17	0.28	0.168	1.34
0.3	0.16	0.27	0.151	1.84
0.5	0.16	0.35	0.189	1.34
0.5	0.10	0.32	0.173	1.84

noise. The picture is somewhat more complicated in redshift space, since the RSD enhancement on linear scales depends on β , and there is a decrease on small scales. Additionally, we expect biased tracers to display a different BAO signal than the mass field (Angulo et al. 2012; Prada et al. 2016).

We study the effect of the large-scale bias by analysing several samples drawn from the MXXL simulation with different number density, large-scale bias, and redshift errors. We gather the results of the analysis in Table 4. The difference between the large-scale bias of the different samples is small but allow us to extract some conclusions. The first is that the shift in α is compatible with zero at the 1σ level for all the samples. Moreover, it is compatible with the bias obtained from the COLA mocks and thus, the fact that we are studying samples of DM haloes instead of DM particles like in COLA does not introduce any systematic bias in α .

As we commented before, the parameter of our model which controls the suppression of the BAO feature is k_* . We find that the value of k_* is the smallest for the samples with the greatest large-scale bias, where a higher value of k_* means a smaller suppression of the BAO feature. This confirms the analytical predictions of Eq. 29.

We find that σ_α is slightly smaller for samples with greater large-scale bias and redshift errors, being the difference more important for the samples with the smallest number density. This is because a higher large-scale bias reduces the rel-

ative contribution of the shot-noise to the power spectrum monopole.

The large-scale bias also modifies the cosmological information encoded in α , since a higher bias decreases the dependence of the BAO scale on the Hubble parameter (see Table 1).

5.4 Analytical estimation of σ_α

In the previous subsections we explored the dependence of σ_α on the redshift errors, the number density, and the large-scale bias b . We showed that their net effect can be understood in terms of their impact on the overall amplitude of the power spectrum with respect to the shot noise. Therefore, we expect that a good predictor for the error recovering the BAO scale be proportional to the total signal-to-noise encoded in a particular configuration. We thus write

$$\tilde{\sigma}_\alpha = A \left(\int dk \frac{P_0 G_{\text{eff}}}{\sigma[P_0]} \right)^{-1}, \quad (41)$$

similarly to Eq. 37, the lower limit of the integral is set to $0.05 h\text{Mpc}^{-1}$ and the upper limit to $0.3 h\text{Mpc}^{-1}$. We compute the value of the normalization constant $A = 6.5 h\text{Mpc}^{-1}$ by fitting the values retrieved by our previous MCMC analyses. We recall that we provided analytical expressions for the power spectrum monopole, P_0 , and its variance, $\sigma[P_0]$, in §3.1 and §3.2, respectively.

We can appreciate the performance of this model in Fig. 9, whose predictions are displayed as coloured lines. We can see that our model captures qualitatively the behaviour of the measured uncertainties in α .

5.5 Effect of the PDF of redshift errors

In the previous sections we have modelled redshift errors as Gaussian distributions. However, this might not be necessarily a good approximation to reality under some circumstances. Therefore, to finalize our paper we explore the performance of our fitting procedure when considering different probability distribution functions with varying levels of skewness and kurtosis (see §2.3).

Fig. 10 shows the best fit values of α from the COLA ensemble with different PDFs for redshift errors and for $\bar{n} = 10^{-2} h^3\text{Mpc}^{-3}$. Shaded regions denote the 68 % and 95 % confidence levels for a Gaussian PDF with $\sigma_z/(1+z) = 0.3\%$. The x -axis indicates the excess kurtosis of each distribution. Note that we plot the Cauchy distribution at a excess kurtosis of 9 (the actual value is not defined). Note also that the skewness

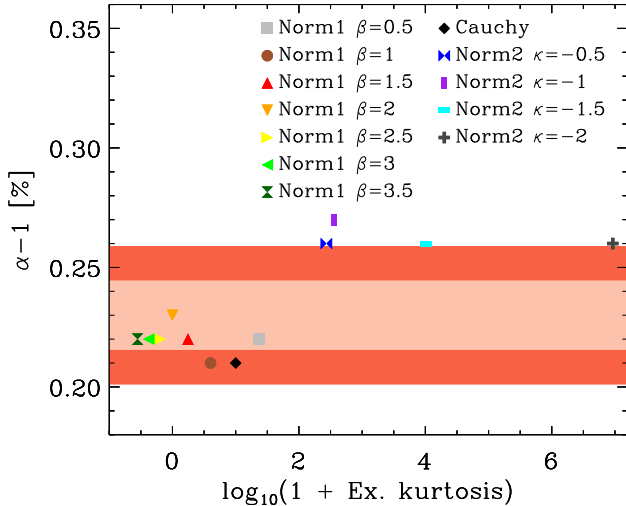


Figure 10. Shift of the BAO scale computed from the average power spectrum of the COLA ensemble with redshift errors following different PDFs as indicated by the legend. The difference between the 84th and 16th percentile of the different PDFs is $2\sigma_z$, where $\sigma_z/(1+z) = 0.3\%$. The coloured areas encloses the 1σ and 2σ regions for redshift errors following a Gaussian distribution. We introduce these families of distributions in §2.3.

is zero for the family Norm1. For the family Norm2, it goes from 1.73 for $\kappa = 0.5$ to 416.9 for $\kappa = 2.0$.

We can see that the recovered BAO scale is largely insensitive to the actual PDF shape at the statistical level of our simulated catalogues – all but one case is compatible with the Gaussian case at the 2σ level. In light of the discussion presented in §4.1, we expect that the effect of different PDFs be to change the weighted average of $G(k, \mu)$. For extreme PDFs, this could in principle introduce systematic errors in the estimation of α . In practice, however, we expect that a reasonable estimate of the redshift error PDF would allow the construction of an unbiased estimator.

6 CONCLUSIONS

We have presented a detailed study of the effect of redshift uncertainties on the galaxy clustering, with an emphasis on the BAO signal. Our main findings can be summarized as follows:

- We provide analytical expressions for the impact of redshift errors on the shape and variance of the redshift-space power spectrum monopole and quadrupole. In Figs. 1 and 2, we show that these capture the relevant modifications and that they agree with results from N -body simulations within 5% up to $k = 0.6 h \text{ Mpc}^{-1}$.
- We show analytically and with simulations that redshift errors in redshift space make the BAO feature *sharper* (Fig. 4). This is because redshift uncertainties reduce the weight of Fourier modes parallel to the line-of-sight, which display a more diluted BAO signal due to non-linear RSD.
- We compute explicitly the dependence of the cosmological information encoded on the BAO on redshift errors, redshift-space distortions, and number density of the galaxy sample considered. We show in Fig. 5 the degeneracy between the

error in $H(z)$ and $D_A(z)$ for samples with different configurations.

- Based on those findings, we build a model for extracting the BAO information from the spherically-averaged power spectrum. We then apply this model to simulated galaxy catalogues with different levels of shot noise, large-scale bias, and redshift errors. For all of them we find that redshift errors do not significantly shift the BAO with respect to the case without redshift errors.

- We find that the error in α depends on the sharpness of the BAO and the relative amplitude of the power spectrum monopole with respect to the shot noise, showing that the error in α is smaller for samples with $\sigma_z/(1+z) < 0.4\%$ and $n > 3 \times 10^{-3} h^3 \text{ Mpc}^{-3}$ than for samples with no redshift errors.

- In §5.5 we consider different PDF the redshift errors. We display in Fig. 10 our findings which suggest that our BAO estimator is robust against different PDFs of redshift errors.

- Finally, in Eq. 41 we provide a quick method to forecast the uncertainty on the BAO scale based on analytical expressions provided in this paper.

We have probed that it is crucial a profound understanding of the effect of redshift errors on the galaxy clustering to extract correctly the BAO scale and to understand what combination of cosmological parameters this scale is constraining. We have also demonstrated that samples with smaller errors are not always the best ones to measure the BAO scale, it depends on the number density and the cosmological parameter that we want to constrain. Therefore, it will be very important for photometric surveys to define carefully the galaxy sample employed to compute α .

ACKNOWLEDGEMENTS

We acknowledge discussions with Raul Abramo, Andreu Font-Ribera, Licia Verde, and Carlos López-Sanjuan. The authors acknowledge support from AYA2015-66211-C2-2. J. Chaves-Montero acknowledges support from the Fundación Bancaria Ibercaja for developing this research.

REFERENCES

- Anderson L. et al., 2012, MNRAS, 427, 3435
 Angulo R. E., Baugh C. M., Frenk C. S., Lacey C. G., 2008, MNRAS, 383, 755
 Angulo R. E., Springel V., White S. D. M., Jenkins A., Baugh C. M., Frenk C. S., 2012, MNRAS, 426, 2046
 Angulo R. E., White S. D. M., Springel V., Henriques B., 2014, MNRAS, 442, 2131
 Benítez N. et al., 2009, ApJ, 691, 241
 Blake C., Bridle S., 2005, MNRAS, 363, 1329
 Cai Y.-C., Angulo R. E., Baugh C. M., Cole S., Frenk C. S., Jenkins A., 2009, MNRAS, 395, 1185
 Colombi S., Jaffe A., Novikov D., Pichon C., 2009, MNRAS, 393, 511
 Crocce M., Scoccimarro R., 2008, Phys. Rev. D, 77, 023533
 Dolney D., Jain B., Takada M., 2006, MNRAS, 366, 884
 Eisenstein D. J., Seo H.-J., Sirko E., Spergel D. N., 2007, ApJ, 664, 675
 Eisenstein D. J. et al., 2005, ApJ, 633, 560
 Foreman-Mackey D., Hogg D. W., Lang D., Goodman J., 2013, PASP, 125, 306

- Glazebrook K., Blake C., 2005, *ApJ*, 631, 1
Hartlap J., Simon P., Schneider P., 2007, *A&A*, 464, 399
Howlett C., Manera M., Percival W. J., 2015, *Astronomy and Computing*, 12, 109
Ilbert O. et al., 2009, *ApJ*, 690, 1236
Kaiser N., 1987, *MNRAS*, 227, 1
Koda J., Blake C., Beutler F., Kazin E., Marin F., 2015, *ArXiv e-prints*
Padmanabhan N., White M., 2009, *Phys. Rev. D*, 80, 063508
Percival W. J. et al., 2007, *ApJ*, 657, 51
Percival W. J. et al., 2010, *MNRAS*, 401, 2148
Prada F., Scóccola C. G., Chuang C.-H., Yepes G., Klypin A. A., Kitauro F.-S., Gottlöber S., Zhao C., 2016, *MNRAS*, 458, 613
Ross A. J., Percival W. J., Manera M., 2015, *MNRAS*, 451, 1331
Sánchez A. G., Baugh C. M., Angulo R. E., 2008, *MNRAS*, 390, 1470
Schmittfull M., Feng Y., Beutler F., Sherwin B., Chu M. Y., 2015, *Phys. Rev. D*, 92, 123522
Seo H.-J., Eisenstein D. J., 2003, *ApJ*, 598, 720
Seo H.-J., Eisenstein D. J., 2007, *ApJ*, 665, 14
Serenio M., Veropalumbo A., Marulli F., Covone G., Moscardini L., Cimatti A., 2015, *MNRAS*, 449, 4147
Smith R. E., Scoccimarro R., Sheth R. K., 2008, *Phys. Rev. D*, 77, 043525
Springel V., 2005, *MNRAS*, 364, 1105
Springel V. et al., 2005, *Nature*, 435, 629
Tassev S., Zaldarriaga M., Eisenstein D. J., 2013, *JCAP*, 6, 036
Weinberg D. H., Mortonson M. J., Eisenstein D. J., Hirata C., Riess A. G., Rozo E., 2013, *Phys. Rep.*, 530, 87

APPENDIX A:

The expressions we provided in the main body of this paper diverge as $k\sigma_{\text{eff}} \rightarrow 0$. However, by expanding the exponential functions into a power series, we find alternative expressions:

$$\langle \mathcal{F}^2 \rangle = \sum_{j=0}^{\infty} (-1)^j \frac{(k\sigma_{\text{eff}})^{2j}}{j!} \left(\frac{1}{2j+1} + \frac{2\beta}{2j+3} + \frac{\beta^2}{2j+5} \right), \quad (\text{A1})$$

$$\langle \mu^2 \mathcal{F}^2 \rangle = \sum_{j=0}^{\infty} (-1)^j \frac{(k\sigma_{\text{eff}})^{2j}}{j!} \left(\frac{1}{2j+3} + \frac{2\beta}{2j+5} + \frac{\beta^2}{2j+7} \right), \quad (\text{A2})$$

$$\langle \mathcal{F}^4 \rangle = \sum_{j=0}^{\infty} (-2)^j \frac{(k\sigma_{\text{eff}})^{2j}}{j!} \left(\frac{1}{2j+1} + \frac{4\beta}{2j+3} + \frac{6\beta^2}{2j+5} + \frac{4\beta^3}{2j+7} + \frac{\beta^4}{2j+9} \right), \quad (\text{A3})$$

$$\langle \mu^2 \mathcal{F}^4 \rangle = \sum_{j=0}^{\infty} (-2)^j \frac{(k\sigma_{\text{eff}})^{2j}}{j!} \left(\frac{1}{2j+3} + \frac{4\beta}{2j+5} + \frac{6\beta^2}{2j+7} + \frac{4\beta^3}{2j+9} + \frac{\beta^4}{2j+11} \right), \quad (\text{A4})$$

$$\langle \mu^4 \mathcal{F}^4 \rangle = \sum_{j=0}^{\infty} (-2)^j \frac{(k\sigma_{\text{eff}})^{2j}}{j!} \left(\frac{1}{2j+5} + \frac{4\beta}{2j+7} + \frac{6\beta^2}{2j+9} + \frac{4\beta^3}{2j+11} + \frac{\beta^4}{2j+13} \right), \quad (\text{A5})$$

$$\langle G(k, \mu) \mathcal{F}^2 \rangle = e^{-\frac{1}{2}(k\sigma_{\perp})^2} \sum_{j=0}^{\infty} (-1)^j \frac{u^{2j}}{j!} \left(\frac{1}{2j+1} + \frac{2\beta}{2j+3} + \frac{\beta^2}{2j+5} \right), \quad (\text{A6})$$

where $u = k\sqrt{\sigma_{\text{eff}}^2 + (\sigma_{\parallel}^2 - \sigma_{\perp}^2)/2}$. We employ these expressions for $k\sigma_{\text{eff}} \leq 3$ ($u \leq 3$) and the expressions provided in the main body of this paper for $k\sigma_{\text{eff}} > 3$ ($u > 3$).

APPENDIX B: EFFECT OF NON-DIAGONAL TERMS IN COVARIANCE MATRICES

In §3 we derive analytically the covariance matrix of the power spectrum monopole, where non-diagonal terms are zero because we assume that the matter density field is Gaussian. However, this approximation breaks on non-linear scales, where non-linearities couples different k -modes. In this section we estimate the validity of this assumption using N -body simulations.

We employ in §5 precision matrices estimated from ensembles of 300 COLA simulations. We correct those precision matrices by a prefactor introduced by Hartlap et al. (2007), as we mention in §2.2. We check that the relative difference between the diagonal terms of the corrected covariance matrices and the diagonal terms of the precision matrices computed inverting Eq. 16 is within 5%.

We check whether non-diagonal terms modify α or its error in §5 using analytical precision matrices. We find that the relative difference between the new and old values is within 4% and thus, non-diagonal terms at $z = 1$ are not important in the range of scales that we are using. Therefore, this motivates the use of analytical precision matrices, since they can be computed instantly for different combinations of redshift errors, large-scale biases, number densities, and cosmological parameters.